NMR Structure and Comparison of the Archaeal Histone HFoB from the Mesophile *Methanobacterium formicicum* with HMfB from the Hyperthermophile *Methanothermus fervidus*†

Wenlian Zhu,‡ Kathleen Sandman,§ Grace E. Lee,‡ John N. Reeve,*,§ and Michael F. Summers*,‡

Howard Hughes Medical Institute and Department of Chemistry and Biochemistry, University of Maryland Baltimore County, 1000 Hilltop Circle, Baltimore, Maryland 21250, and Department of Microbiology, The Ohio State University, Columbus, Ohio 43210

Received December 8, 1997; Revised Manuscript Received March 27, 1998

ABSTRACT: The solution-state structure of the recombinant archaeal histone rHFoB, from the mesophile *Methanobacterium formicicum*, has been determined by two- and three-dimensional (3D) proton homonuclear correlated nuclear magnetic resonance (NMR) methods. On the basis of 951 nuclear Overhauser effect (NOE)-derived distance restraints, rHFoB monomers form the histone fold and assemble into symmetric $(rHFoB)_2$ dimers that have a structure consistent with assembly into archaeal nucleosomes. rHFoB exhibits ∼78% sequence homology with rHMfB from the hyperthermophile *Methanothermus fervidus*, and the results obtained demonstrate that these two proteins have very similar 3D structures, with a root-mean-square deviation for backbone atoms of 0.65 ± 0.13 Å^2. $(rHFoB)_2$ dimers however unfold at lower temperatures and require a higher salt environment for stability than $(rHMfB)_2$ dimers, and comparing the structures, we predict that these differences result from unfavorable surface-located ionic interactions and a larger, more solvent-accessible cavity adjacent to residue G36 in the hydrophobic core of $(rHFoB)_2$.

Archaeal histones are small, basic DNA-binding proteins that share a common ancestry with the eukaryal nucleosome core histones, H2A, H2B, H3, and H4 (*1*). Consistent with this heritage, they wrap DNA into nucleosome-like structures both in vitro and in vivo (*2*, *3*). Eighteen archaeal histone sequences have been determined (*1*). They range in length from 66 to 69 residues and are 60−95% identical in sequence, and members of this family have been purified and characterized from mesophilic, thermophilic, and hyperthermophilic *Archaea*. The structure of recombinant (r) HMfB,[1] synthesized in *Escherichia coli* by expression of the *hmfB* gene cloned from the hyperthermophile *Methanothermus fervidus* (optimum growth temperature of 83 °C), has been established (*4*) and shown to conform to the histone fold (*5*). On the basis of the high conservation in amino acid sequences, it seems likely that all archaeal histones retain this fold; however, they exhibit differences in DNA binding and compaction (*6*), and in salt dependency and thermal stability (*7*−*9*).

Since the discovery of hyperthermophiles, comparing the structures of related proteins from mesophiles and hyperthermophiles has become an attractive approach for identifying thermostability-conferring features. However, in most cases, the conclusions are limited by the relatively large sizes and low sequence identities of the proteins being compared (*10*−*16*). In contrast, rHFoB, the recombinant version of HFoB from the mesophile *Methanobacterium formicicum*

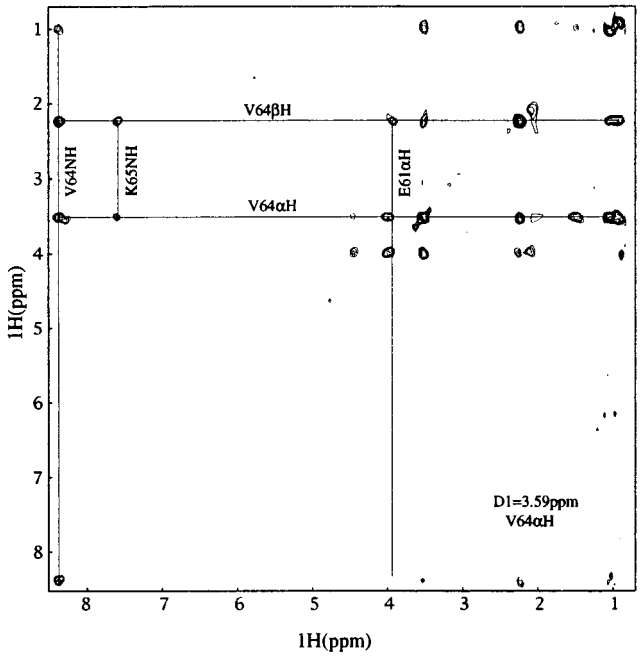

FIGURE 1: D2D3 plane of the 3D NOESY−HOHAHA spectrum at the α-proton of V64. The peak at the intersection of V64 $^{\beta}$C and A61 $^{\alpha}$H is the NOE cross-peak between E61 $^{\alpha}$H and V64 $^{\alpha}$H following the path V64 $^{\alpha}$H →(*J*) V64 $^{\beta}$H →(NOE) E61 $^{\alpha}$H.

† This work was supported by NIH Grant GM53185.

* Corresponding authors. M.F.S. e-mail: summers@hhmi.umbc.edu. J.N.R. e-mail: reeve.2@osu.edu.

‡ University of Maryland Baltimore County.

§ The Ohio State University.

[1] Abbreviations: HFo, histone from *Methanobacterium formicicum*; HMf, histone from *Methanothermus fervidus*; HPy, histone from *Pyrococcus* strain GB-3a; HMt, histone from *Methanobacterium thermoautotrophicum*; 2D, two-dimensional; 3D, three-dimensional; DQF, double quantum filter; COSY, scalar correlation spectroscopy; HOHAHA, homonuclear Hartmann−Hahn spectroscopy; NOE, nuclear Overhauser effect; NOESY, nuclear Overhauser effect spectroscopy.

S0006-2960(97)03007-9 CCC: $15.00
Published on Web 07/07/1998

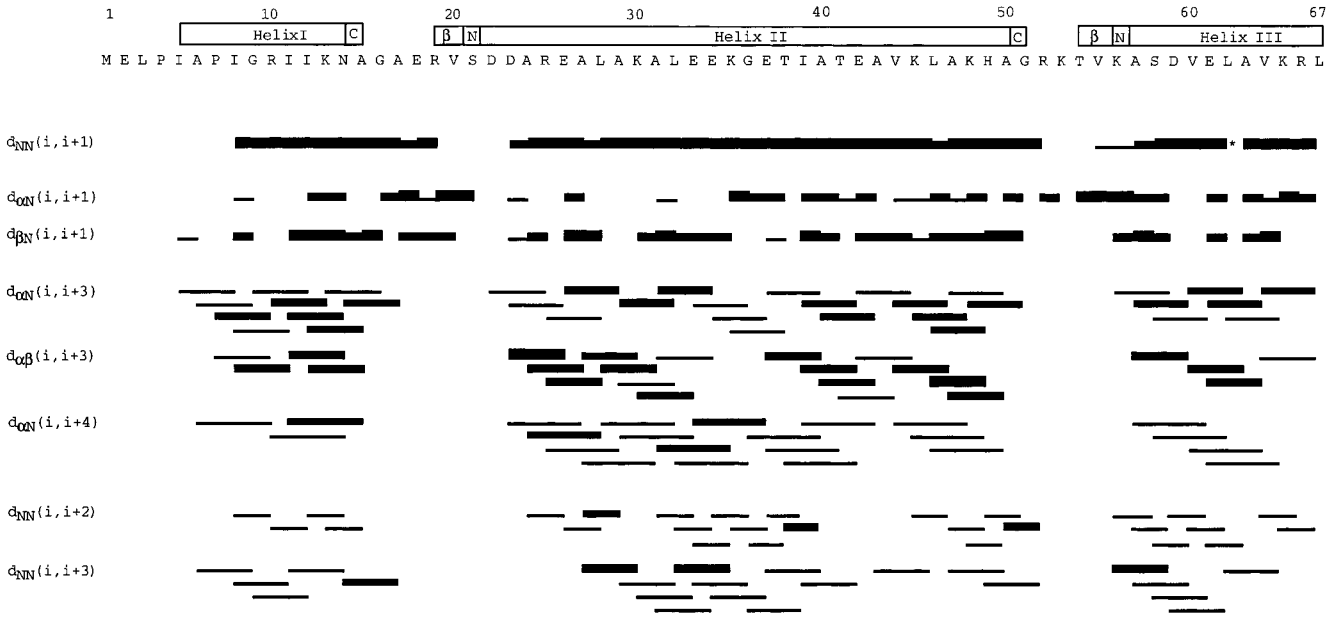

FIGURE 2: Summary of the NOE connectivities for backbone atoms of rHFoB. The α-helical regions are indicated by boxes with the N-cap and C-cap residues designated N and C, respectively. Strong, medium, and weak NOE connectivities are indicated by thick, medium, and thin bars, respectively. Chemical shift overlaps prevented the assignment of specified connectivities (indicated with asterisks).

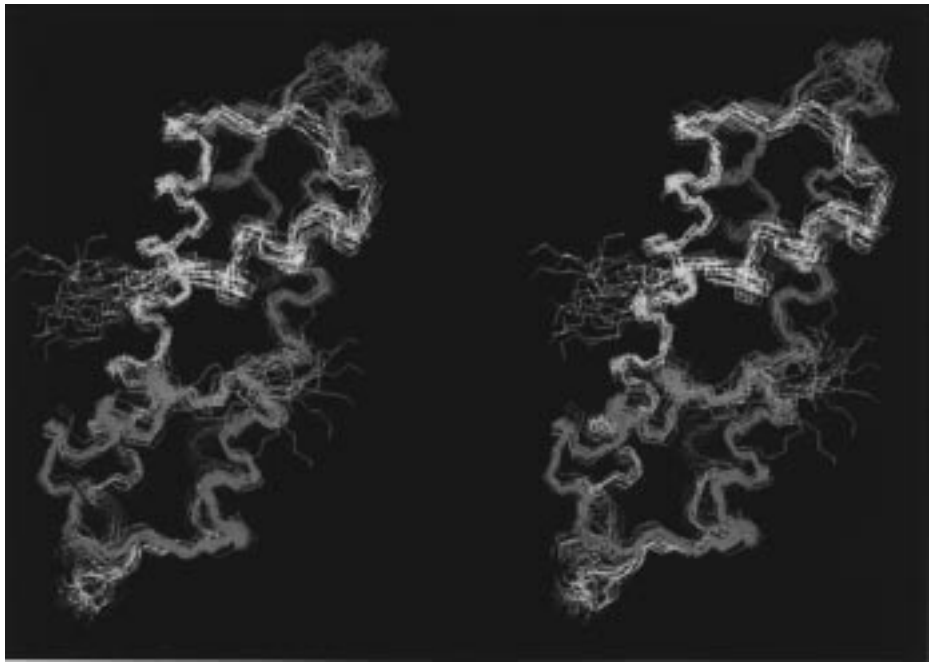

FIGURE 3: Best-fit superposition of backbone heavy atoms (C, C^{α}, and N) of the 19 models of the $(rHFoB)_2$ dimer. Individual monomers are shown in blue and cyan.

[optimum growth temperature of 43 °C (*7*)], and rHMfB contain only 67 and 69 amino acid residues, respectively, in sequences that differ at only 15 locations (78% identical). Only six of these differences are nonconservative changes, and yet under identical solution conditions, rHFoB molecules unfold at temperatures >30 °C lower than the temperatures at which rHMfB molecules unfold (*8*). To confirm that rHFoB forms the histone fold, and to provide the structural foundation needed to identify the molecular determinants of this difference in stability, we have established the 3D structure of the $(rHFoB)_2$ dimer by NMR methods. Here we report this structure and a comparison with the structure of the $(rHMfB)_2$ dimer (*4*).

MATERIALS AND METHODS

Preparation of rHFoB. Induction of rHFoB synthesis and purification of rHFoB from *E. coli* JM105 (pKS406) have been described (*8*). rHFoB solutions were prepared for NMR spectroscopy at ∼1 mM monomer concentrations in ∼50 mM *d*-acetate (99% d_3-acetate), 2 mM NaH_2PO_4, and 1 M NaCl (pH 6), as described for rHMfB (*4*).

NMR Spectroscopy. NMR data were collected with a GE OMEGA-PSG 600 NMR spectrometer at sample temperatures of 25, 35, and 45 °C. Quadrature detection, in the indirect dimensions, was accomplished by using the States−TPPI technique (*17*, *18*). Data were collected with a spectral

Table 1: Summary of ^{1}H NMR Chemical Shifts Observed for rHFoB at 35 °C

residue		NH	αH	βH	others
1	Met				
2	Glu				
3	Leu	8.588	4.426	2.004, 1.931	γ 1.265; δ 0.798
4	Pro		4.624		βγ 2.098, 2.012; δ 3.500, 3.975
5	Ile	7.865	3.912	1.895	γ 1.394; γCH$_3$ 0.926; δCH$_3$ 0.837
6	Ala	8.814	4.386	1.589	
7	Pro		4.316	1.650, 2.608	γ 2.012, 2.108; δ 3.724, 3.819
8	Ile	6.882	3.729	2.358	γ 1.468, 1.391; γCH$_3$ 1.065; δCH$_3$ 0.819
9	Gly	8.255	3.620, 4.152		
10	Arg	7.513	4.029	2.058	γ 1.633, 1.854; δ 3.263, 3.361; ϵ 7.778
11	Ile	7.679	3.748	2.093	γ 1.186, 1.935; γCH$_3$ 0.781; δCH$_3$ 0.871
12	Ile	7.371	3.750	1.935	γ 0.618, 2.029; γCH$_3$ 0.873; δCH$_3$ 0.755
13	Lys	8.049	4.150		
14	Asn	8.865	4.472	2.902, 3.035	
15	Ala	7.495	4.466	1.563	
16	Gly	7.868	3.748, 4.479		
17	Ala	7.179	4.329	1.204	
18	Glu	9.318	4.211	2.212	γ 2.290, 2.432
19	Arg	7.580	4.628	1.596, 1.811	
20	Val	8.740	4.398	2.019	γCH$_3$ 0.822, 1.011
21	Ser	8.454	4.668	4.009, 4.386	
22	Asp	9.159	4.420	2.812, 2.771	
23	Asp	8.748	4.491	2.855	
24	Ala	8.096	3.816	1.340	
25	Arg	7.467	3.800	2.146	γ 1.397, 1.977; δ 3.209, 3.345; ϵ 7.303
26	Glu	7.860		2.123	γ 2.310, 2.426
27	Ala	8.063	4.226	1.547	
28	Leu	8.179	4.160	1.363, 1.981	γ 1.628; δCH$_3$ 0.921, 1.055
29	Ala	8.336	3.909	1.545	
30	Lys	8.334	4.031	1.954	
31	Ala	7.787	4.317	1.535	
32	Leu	8.526	4.089	1.936, 2.006	γ 1.628; δCH$_3$ 0.797
33	Glu	8.668	3.806	2.217, 2.423	γ 2.363
34	Glu	8.120	4.128	2.178, 2.232	γ 2.330, 2.583
35	Lys	8.031	4.396	1.789	
36	Gly	9.132	3.647, 3.771		
37	Glu	8.759	3.979	2.331	γ 2.521, 2.712
38	Thr	8.159	4.072	4.408	γCH$_3$ 1.406
39	Ile	8.501	3.587	1.806	γ 1.968; γCH$_3$ 0.886; δCH$_3$ 0.776
40	Ala	8.900	3.839	1.469	
41	Thr	8.383	3.901	4.447	γCH$_3$ 1.403
42	Glu	7.601	4.266	2.202	γ 2.464, 2.341
43	Ala	8.867	4.054	1.366	
44	Val	8.390	3.506	2.226	γCH$_3$ 1.023, 0.907
45	Lys	7.614	3.979	1.976	γ 1.377, 1.721
46	Leu	8.382	4.042	1.602, 2.158	γ 1.968; δCH$_3$| 0.921, 1.054
47	Ala	8.248	4.106	1.472	
48	Lys	8.403	4.206	1.998	γ 1.686, 1.737
49	His	8.622	4.468	3.440	
50	Ala	7.708	4.463	1.686	
51	Gly	8.018	3.857, 4.160		
52	Arg	8.176	4.656		δ 3.110, 3.467; ϵ 7.110
53	Lys	8.355	4.381		
54	Thr	7.419	4.613	4.019	γCH$_3$ 1.065
55	Val	8.032	4.163	1.838	γCH$_3$ 1.012, 1.052
56	Lys	9.633	5.082	1.558, 1.730	γ 2.211; ϵ 3.035
57	Ala	8.797	3.733	1.374	
58	Ser	8.328	4.125	3.867, 3.946	
59	Asp	7.091	4.492	3.030, 3.199	
60	Val	7.183	3.380	2.232	γCH$_3$ 0.744, 0.963
61	Glu	8.754	3.873	2.046	g 2.246, 2.406
62	Leu	7.817	4.175	1.684, 1.830	γ 1.735; δCH$_3$ 0.987, 1.002
63	Ala	7.817	3.964	1.609	
64	Val	8.311	3.594	2.235	
65	Lys	7.479	4.186	1.736, 2.037	
66	Arg	7.629	4.371	2.057	γ 1.760, 1.832; δ 3.164, 3.201; ϵ 7.433
67	Leu	7.265	4.227	1.674	γ 1.925; δCH$_3$ 0.901

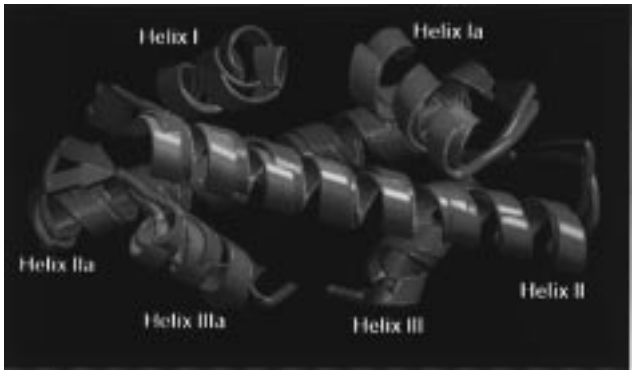

FIGURE 4: Best-fit superposition of backbone heavy atoms (C, C$^\alpha$, and N) of the lowest-penalty structures of rHFoB (red) and rHMfB (green) generated by using the MidasPlus software package.

width of 7017.5 Hz in all dimensions. Water suppression was achieved with a continuous-wave irradiation presaturation period of 1.2 s, followed by a 40 ms SCUBA sequence to allow recovery of saturated protons at water frequency. 2D NOESY data (*19*, *20*) were collected with mixing times of 120, 150, and 200 ms. 2D HOHAHA data (*21*, *22*) were collected in the "clean" mode (*23*) with an 80 ms MLEV-17 spin-lock sequence flanked by 1 ms trim pulses. 2D DQF-COSY data (*24*) were collected at all three temperatures. 3D NOESY−HOHAHA data (*25*) were recorded at 35 °C with 64 t_1 (NOESY) and 37 t_2 (HOHAHA) complex points. All data were transferred via ethernet to Silicon Graphics computers for processing and analysis with the FELIX (v2.3, Biosym Technologies, Inc.) and NMRVIEW (*26*) software packages.

Structure Calculations. Structure calculations were performed using the program DIANA following the REDAC minimization strategy (*27*). Only functional NOEs were employed for the structure calculations, and many intraresidue and redundant NOEs were not used. For example, in cases where a proton exhibited a NOE to one prochiral proton or methyl group, and a weaker NOE to the other prochiral group, then restraints were employed for only the stronger of the two NOEs. In addition, intraresidue distance restraints were not employed for protons on most of the exposed, charged side chains as these groups are likely to be undergoing rapid conformational averaging on the NMR chemical shift time scale. NOE cross-peaks were classified as strong, medium, and weak, and corresponding upper-limit distance restraints of 2.7, 3.3, and 5.0 Å were assigned. To allow for maximal conformational sampling, upper distance limits of 2.9 and 3.5 Å were employed for strong-intensity sequential and medium-intensity NH−NH cross-peaks. The upper limits were extended by 0.8, 0.5, and 1.5 Å for NOEs involving methylene, methyl, and phenyl pseudoatoms, respectively. Backbone NH−O hydrogen bond restraints were employed for the helical elements identified via secondary structure analysis of the NOE cross-peak patterns. A total of four restraints were employed per hydrogen bond, including upper distance limits of 2.0 and 3.0 Å and lower distance limits of 1.8 and 2.7 Å for the NH−ON−O atom pairs, respectively.

RESULTS

Analysis of the NMR Data. ^{1}H NMR signal assignments were made using standard sequential assignment strategies

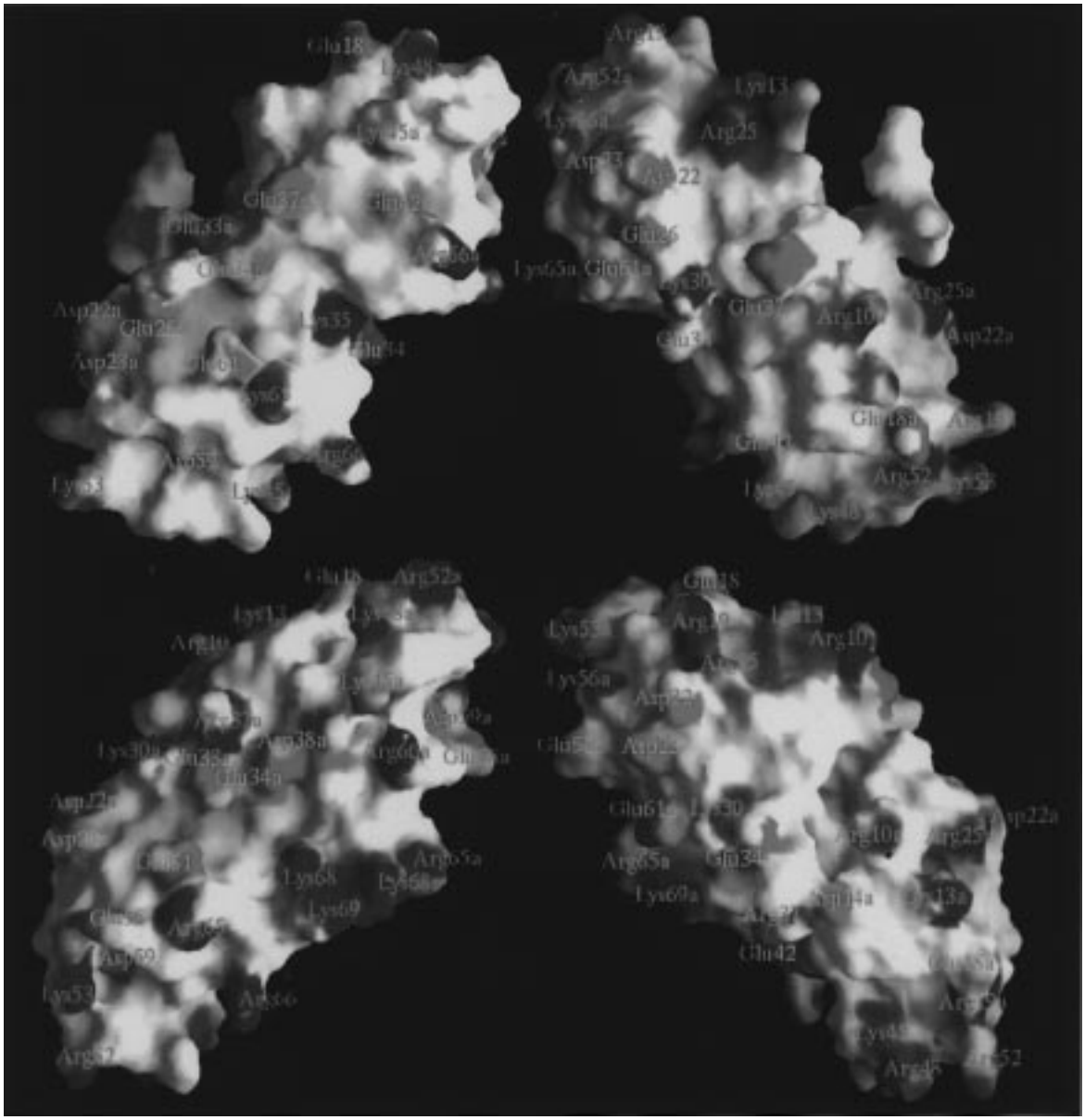

FIGURE 5: Surface maps of the electrostatic potential of $(rHFoB)_2$ and $(rHMfB)_2$ dimers generated by GRASP (*39*). Positive surface potential is shown in blue and negative surface potential in red. The upper images are rHFoB, and the lower images are rHMfB. The right images differ from the left images by a 180° rotation.

(*28*). Overlapping signals in 2D NOESY, DQF-COSY, and TOCSY spectra were assigned by comparing data collected at different temperatures, and by the analysis of 3D NOESY−TOCSY data. For example, assignment of the E61 $C^{\alpha}H$−V64 $C^{\alpha}H$ cross-peak could not be made from the 2D NOESY spectra due to overlap of one of the E61 $C^{\alpha}H$ and V64 $C^{\alpha}H$ protons. However, an intense E61 $C^{\alpha}H$−V64 $C^{\alpha}H$ cross-peak was unambiguously assigned in the 3D NOESY−TOCSY spectrum (Figure 1). The proton NMR chemical shift assignments made at 35 °C are summarized in Table 1.

Short- and medium-range NOE connectivities, observed in the 2D NOESY and 3D NOESY−TOCSY spectra, are summarized in Figure 2. The NOE data indicate that rHFoB monomers contain three α-helices, designated I, II, and III formed by I5−A15, D22−A50, and A57−L67, respectively, characterized by stretches of intense $d_{NN}(i,i+1)$, weak $d_{NN}(i,i+2)$, medium $d_{\alpha\alpha}(i,i+3)$, weak $d_{\alpha N}(i,i+3)$, and weak $d_{\alpha N}(i,i+4)$ NOE cross-peaks. Amide protons of residues M1 and E2 were not observed due to rapid exchange with water protons.

Helices II and III contain N-terminal caps, as indicated by weak $d_{NN}(i,i+3)$ and moderate $d_{N\alpha}(i,i+3)$ NOEs in S21-(N_{CAP})−A24, moderate $d_{\alpha N}(i,i+1)$ NOEs for S21-D22, and strong $d_{\alpha N}(i,i+1)$ NOEs for K56(N_{CAP})-A57. Schellman C-terminal capping motifs were identified for helices I and II, for the positions designated as C3-C2-C1-C_{CAP}-C′(Gly)-C″, based on medium to strong $d_{\alpha N}(i,i+4)$ NOEs between the C2 and C″ residues (K13−A17 and K48−R52). The C-terminal residue of helix III (L67) is the C-terminal residue of the polypeptide.

Strong-intensity $d_{\alpha N}(i,i+1)$ NOEs were observed for residues A17-E18, R19-V20, V20-S21, T54-V55, V55-K56, and K56-A57, as well as long-range NOE cross-peaks for the following proton pairs: T54 αH−R19 NH, V55 NH−R19 NH, and V55 NH−S21 NH. Residues R19-V20-S21 and T54-V55 are located in β-strand loops between helices I and II and between helices II and III, respectively, and

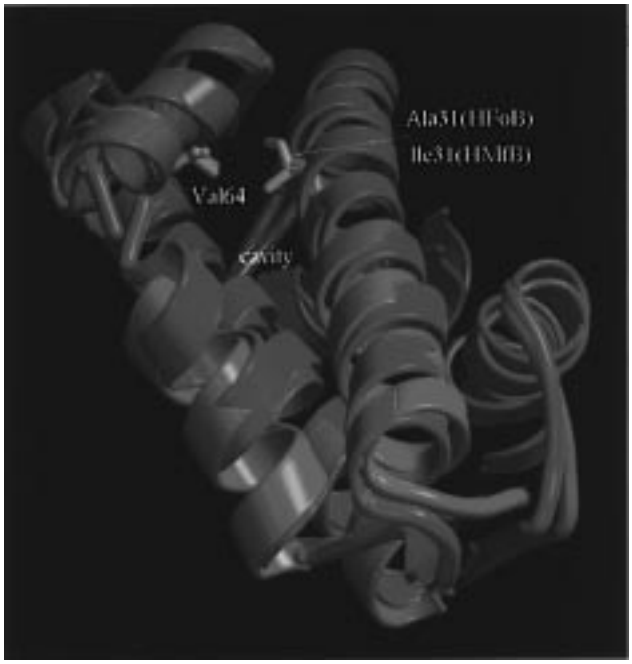

FIGURE 6: Ribbon representations of $(rHFoB)_2$ and $(rHMfB)_2$ dimers generated by MOLSCRIPT (*47*) and rendered with Raster 3D (*48*). rHFoB is shown in red and rHMfB in green, with side chains surrounding the cavity in $(rHFoB)_2$ indicated by lighter shades.

interloop connectivities are consistent with short stretches of parallel β-sheet structure. The locations of the α-helices and the capping elements are summarized at the top of Figure 2. Residues R19 and T54 in rHFoB and in rHMfB are located at the positions occupied by R83 and T118 in *Xenopus* histone H3 and R45 and T80 in *Xenopus* histone H4, respectively, and R83 (H3)−T80 (H4) and R45 (H4)−T118 (H3) also interact directly within the paired loop regions that separate helices I and II, and II and III, in an H3−H4 dimer, respectively (*29*). These interactions direct the insertion of the side chains of R83 (H3) and R45 (H4) into the minor groove of the DNA molecule wrapped around a nucleosome, and consistent with archaeal histones employing the same mechanism of DNA binding, rHMfB variants constructed with other residues at position 19 or 54 do not bind DNA (K. Sandman and J. N. Reeve, unpublished results)

Many of the long-range NOE cross-peaks observed in the homonuclear NMR data could only be explained in terms of a $(rHFoB)_2$ dimer. For example, the long-range NOEs from residues in the R19−S21 region to residues in the T54−K56 region cannot be intramonomer as these residues are located at opposite ends of helix II (Figure 2), and the NOE contacts between L28 and I39, L28 and A40, and L28 and V44 are similarly only realistically explicable in terms of intermonomer contacts between two antiparallel, aligned α-helices II. Several additional intermonomer NOE cross-peaks were assigned by a reiterative approach in which an initial structure was calculated on the basis of unambiguously assigned NOEs, and additional cross-peaks were then evaluated in terms of their consistency with this structure (*30*−*32*).

As previously documented for rHMfB (*4*), only one set of signals was observed for all rHFoB protons, consistent with monomers associating to form symmetric $(rHFoB)_2$ homodimers in solution. In terms of residue positions, the side chain proton contacts that define the tertiary fold and the $(rHFoB)_2$ structure are almost identical to those in the $(rHMfB)_2$ dimer, except that the side chain of I5 in α-helix I makes contact with E33 of α-helix II in rHFoB, whereas I5 contacts I26 in rHMfB.

3D Structure Calculations. A total of 951 interproton distance restraints were derived from the 2D and 3D homonuclear correlated NOE data, corresponding to ~14.2 restraints per refined residue. These included 11 intraresidue, 212 sequential, 356 medium-range, 94 long-range (residues >5 Å apart), and 98 intermolecular restraints. Restraints for a total of 45 hydrogen bonds per monomer were also included for each of the three α-helices. Pseudoatom restraints were employed for most β-methylene protons. However, most diastereotopic methyl groups and glycine H^{α} protons were stereochemically assigned, and the appropriate distance restraints were employed. A total of 500 initial starting models with randomly generated initial torsion angles were subjected to conjugate gradient minimization. Minimized structures with target functions of 0.5 $Å^2$ or less were selected and subjected to additional rounds of REDAC refinement (*27*), which ultimately afforded 19 structures with target functions ranging from 0.023 to 0.045 $Å^2$. Best-fit superposition of the backbone heavy atoms of these final structures (residues 5−67 of both monomers) afforded pairwise root-mean-square deviations of 0.65 ± 0.13 Å (Figure 3).

Structure Description and Comparison of $(rHFoB)_2$ with $(rHMfB)_2$. Using the convention established for $(rHMfB)_2$ dimers (*4*), the helices in one rHFoB monomer are referred as I, II, and III, and their homologues in the second monomer in a $(rHFoB)_2$ dimer as Ia, IIa, and IIIa. Due to rapid proton exchange, structure could not established for M1 or E2, and severe proton overlap precluded the observation of the proline cap motif documented for helix I in rHMfB (*4*). As in $(rHMfB)_2$, helices II and IIa in the $(rHFoB)_2$ dimer are aligned in an antiparallel arrangement, and helices I and Ia, and III and IIIa, cross helices II and IIa (Figure 3). A network of hydrophobic contacts is formed between L28 and I39a, L28 and A40a, L28 and V44a, and L32 and G36a and the reciprocal partnerships, L28a and I39, etc., along the interface between helices II and IIa.

I5 of helix I contacts E33 of helix II; A15, the C-cap residue of helix I, makes contacts with A40a and T41a of helix IIa, and A17, located in the C-cap region of helix I, formed connectivities with V44a of helix IIa. I8, I12, and A15 are all located on the same face of helix I and make extensive hydrophobic contacts with residues in helices II and IIa that together contribute substantially to the hydrophobic core. Helix III also extends across helices II and IIa, but in the opposite direction from helix I. A57, the first hydrophobic residue in helix III, contacts A24a and A27a of helix IIa, and the C-terminal residue of helix III, L67, interacts with T38 and I39 of helix II. Additional hydrophobic connectivities involving helix III residues were detected between V60 and L28a, V60 and A43, A63 and I39, and V64 and A31a.

Residues V20 and V55, located in the loop regions between helices I and II, and between helices II and III, respectively, also contribute to the hydrophobic core. V20 makes intramonomer contacts with I12 and A17, whereas

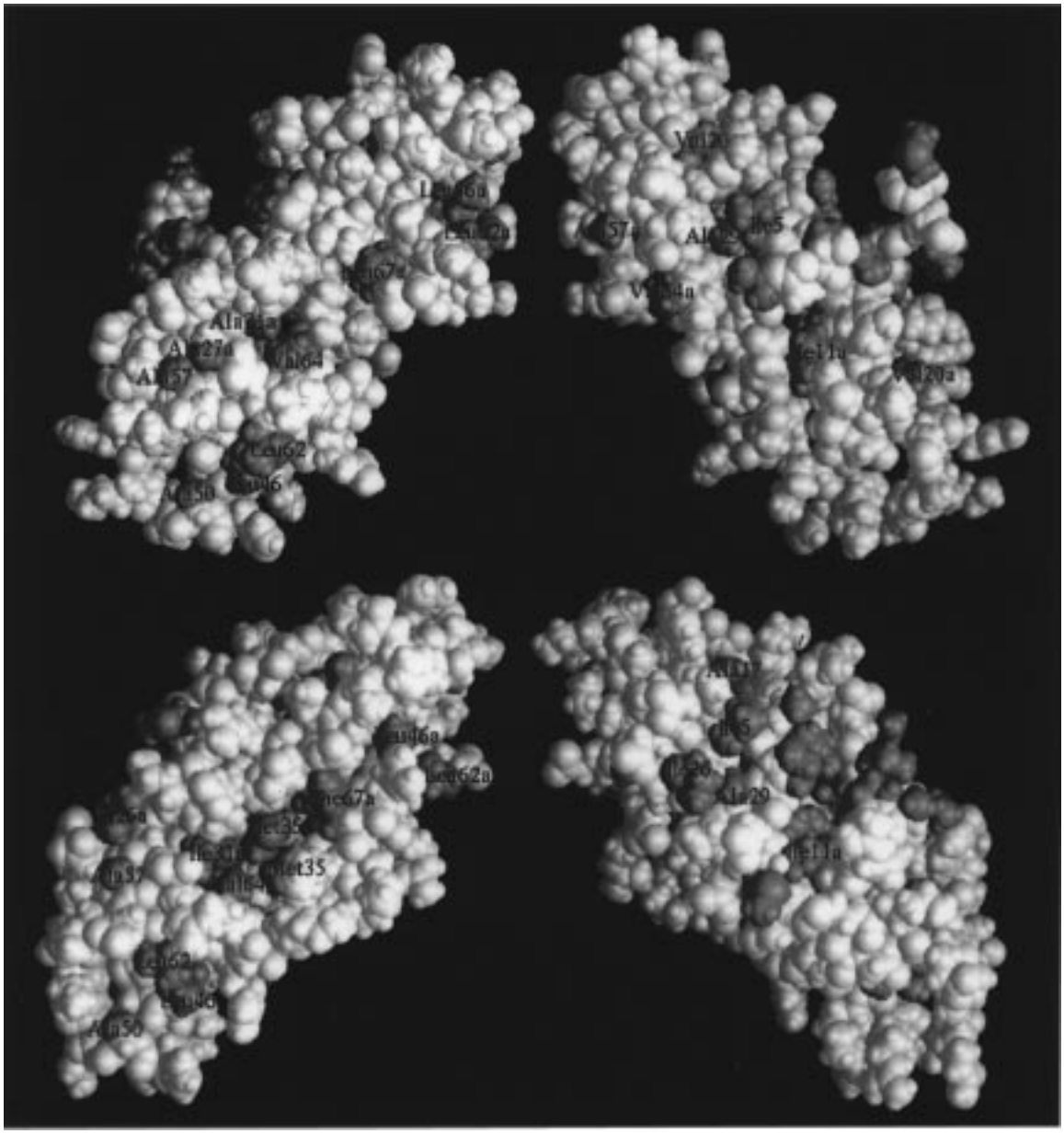

FIGURE 7: Space filling representations of $(rHFoB)_2$ and $(rHMfB)_2$ generated by GRASP (*39*). Hydrophobic residues are shown in green. The upper images are rHFoB, and the lower images are rHMfB. The right images differ from the left images by a 180° rotation.

V55 makes intramonomer contacts with V60 of helix III and intermonomer contacts with I12a of helix Ia and with A17a.

The 3D structure of $(rHFoB)_2$ is very similar to that of $(rHMfB)_2$, with a root-mean-square deviation for the backbone atoms of 1.40 Å for the $(rHFoB)_2$ and $(rHMfB)_2$ structures with lowest penalties. The helix−helix interfaces in both dimers are dominated by hydrophobic interactions, although, as mentioned, the helix I−helix II intramonomer interaction in rHMfB occurs between I5 and I26 whereas I5 makes contacts with E33 in helix II of rHFoB. This results in a slight change in the orientation of helix I relative to helix II, and presumably the I5−E33 helix I−helix II interaction in rHFoB is weaker than the I5−I26 interaction in rHMfB (Figure 4).

DISCUSSION

rHFoB and rHMfB have amino acid sequences that are ~78% identical, and here we have established that they also have very similar 3D structures that conform to the histone fold (*5*). Both archaeal histones form dimers in solution with structures essentially identical to the structures formed by the globular regions of the eukaryal nucleosome core histones in H3−H4 and H2A−H2B dimers (*5*, *29*). Conserved residues are identically positioned in the archaeal and eukaryal histone dimers that are known to participate in DNA binding and assembly of the eukaryal nucleosome (*29*).

Despite their conserved structures, $(rHFoB)_2$ and $(rHMfB)_2$ dimers unfold under identical solution conditions at temperatures that differ by >30 °C (*8*). rHFoB and rHMfB have almost identical secondary structures, and the hydrogen bonds involving backbone atoms are also very similar. It therefore seems unlikely that differences in these features contribute substantially to the large difference in thermal stability. Partial negative and positive charges located near the N- and C-termini of an α-helix can stabilize the α-helix by interacting favorably with the helix dipole (*33*−*37*), and this appears

to be the case for helices II (D- or E22 and K- or R48) and III (D59 and K- or R65) in all the archaeal histones (*1*). There are two negatively charged residues (E58 in addition to D59) in the first turn of helix III of rHMfB but only one (D59) in helix III of rHFoB, which may be a difference that contributes to the increased stability of rHMfB.

Charged residues (D, E, K, and R) comprise 31−42% of all residues in the archaeal histones, and consistent with salt bridges playing an important role in stabilizing protein structures (*38*), reciprocal changes in the positions of charged residues provide strong evidence for specific, localized ionic interactions. For example, in α-helix II of the HFo and HMt histones, D26 or E26 interacts with K30 whereas K26 is partnered with E30 in the HPy histones (see Figure 1 in ref *8*). Comparing surface-located charged residues at positions *i* and *i*+4 or *i*+3 in α-helices suggests that R37 in rHMfB versus E37 in rHFoB could contribute to both the increased stability and lower salt dependency of rHMfB. A favorable R37−E33 interaction along α-helix II in rHMfB replaced by an unfavorable E37−E33 interaction in rHFoB which, together with the I26 (rHMfB) versus E26 (rHFoB) difference, generates a localized region of net negative charge on the surface of the $(rHFoB)_2$ dimer that is not present on the $(rHMfB)_2$ dimer (Figure 5). The higher salt requirement for stabilization of rHFoB (*8*) may therefore, at least in part, reflect the need for salt screening of these otherwise repulsive, adjacent negative charges.

Hydrophobic interactions predominate in forming the histone fold (*1*, *5*, *29*), and hydrophobic residues at positions 8, 12, 17, 20, 28, 29, 32, 36, 39, 40, 43, 55, and 60 are buried within the core of $(rHFoB)_2$ and $(rHMfB)_2$ dimers. Hydrophobic residues are conserved at these locations in all of the archaeal histones, consistent with a conserved fold and a common mechanism of dimer formation (*1*). Hydrophobic core residues are similarly conserved in rubredoxins with different thermal stabilities (*40*). The fraction of buried carbon atoms is also very similar in indole-3-glycerol phosphate synthases from the hyperthermophile *Sulfolobus solfataricus* and from *E. coli* (*12*) and in glutamate dehydrogenases from the hyperthermophile *Pyrococcus furiosus* and from the mesophile *Clostridium symbiosum* (*14*). Apparently, therefore, the overall packing density of the hydrophobic cores of related proteins with different thermal stabilities can be very similar, and differences in solvent accessibility and in localized cavities within these cores are likely to be the features that correlate with differences in stability. The loss of a methyl or methylene group is expected to result in only a marginal change in overall packing density but may create a cavity that results in a significant decrease in stability (*41*−*46*). Each monomer in the $(rHFoB)_2$ and $(rHMfB)_2$ dimers contains a cavity adjacent to G36; however, this is more adequately filled by the side chains of I31, M35, and V64 in rHMfB than by A31, K35, and V64 in rHFoB (Figures 5−7). Consistent with the importance of filling this cavity for thermal stability, a larger A36 replaces G36 in many of the archaeal histones from hyperthermophiles, several of which also contain bulkier tyrosine or histidine residues at position 31 and isoleucine or leucines at position 64 (see Figure 1 in ref *8*). The cavity is also more solvent-accessible in rHFoB than in rHMfB. The C-terminal residues, K68 and K69, of rHMfB overlap and partially protect this region of the core from solvent exposure, whereas rHFoB terminates at position 67 and therefore lacks this protection. The increased solvent exposure, coupled with the presence of a potentially polar K35 rather than a M35 residue, is likely to contribute substantially to the reduced stability of rHFoB, and consistent with this prediction, a K35M variant of rHFoB has a $T_m°$ that is 14 °C higher than that of wild-type rHFoB whereas the M35K variant of rHMfB has a $T_m°$ that is 17 °C lower than that of wild-type rHMfB (*8*; W.-t. Li and J. N. Reeve, unpublished results).

CONCLUSION

The solution structure of rHFoB has been shown to be very similar to that of rHMfB and to conform to the histone fold. rHFoB monomers associate to form symmetric homodimers with structures homologous to the globular regions of the eukaryal nucleosome core histones (*5*, *29*), and conserved residues are appropriately positioned for DNA binding and assembly of archaeal nucleosomes (*3*). The lower stability and increased salt dependency of $(rHFoB)_2$ dimers appear to result from an increased number of unfavorable, surface-located ionic interactions, from a larger and more solvent-accessible cavity within the hydrophobic core, and possibly from weaker interactions maintaining the helix I−helix II interface.

REFERENCES

1. Reeve, J. N., Sandman, K., and Daniels, C. J. (1997) *Cell 89*, 999−1002.
2. Sandman, K., Krzycki, J. A., Dobrinski, B., Lurz, R., and Reeve, J. N. (1990) *Proc. Natl. Acad. Sci. U.S.A. 87*, 5788−5791.
3. Pereira, S. L., Grayling, R. A., Lurz, R., and Reeve, J. N. (1997) *Proc. Natl. Acad. Sci. U.S.A. 94*, 12633−12637.
4. Starich, M. R., Sandman, K., Reeve, J. N., and Summers, M. F. (1996) *J. Mol. Biol. 255*, 187−203.
5. Arents, G., and Moudrianakis, E. N. (1995) *Proc. Natl. Acad. Sci. U.S.A. 92*, 11170−11174.
6. Sandman, K., Grayling, R. A., Dobrinski, B., Lurz, R., and Reeve, J. N. (1994) *Proc. Natl. Acad. Sci. U.S.A. 91*, 12624−12628.
7. Darcy, T. J., Sandman, K., and Reeve, J. N. (1995) *J. Bacteriol. 177*, 858−860.
8. Li, W.-T., Grayling, R. A., Sandman, K., Edmondson, S., Shriver, J. W., and Reeve, J. N. (1998) *Biochemistry 37*, 10563−10572.
9. Soares, D., Dahlke, I., Li, W.-T., Sandman, K., Hethke, C., Thomm, M., and Reeve, J. N. (1998) *Extremophiles 2*, 75−81.
10. Davies, G. J., Gamblin, S. J., Littlechild, J. A., and Watson, H. C. (1993) *Proteins: Struct., Funct., Genet. 15*, 283−289.
11. Delboni, L. F., Mande, S. C., Rentier-Delrue, F., Mainfroid, V., Turley, S., Vellieux, F. M. D., Martial, J. A., and Hol, W. G. L. (1995) *Protein Sci. 4*, 2594−2604.
12. Hennig, M., Darimont, B., Sterner, R., Kirschner, K., and Jansonius, J. N. (1995) *Structure 3*, 1295−1306.
13. Korndorfer, I., Steipe, B., Huber, R., Tomschy, A., and Jaenicke, R. (1995) *J. Mol. Biol. 246*, 511−521.
14. Yip, K. S. P., Stillman, T. J., Britton, K. L., Artymiuk, P. J., Baker, P. J., Sedelnikova, S. E., Engel, P. C., Pasquo, A., Chiaraluce, R., Consalvi, V., Scandurra, R., and Rice, D. W. (1995) *Structure 3*, 1147−1158.
15. DeDecker, B. S., O'Brien, R., Fleming, P. J., Geiger, J. H., Jackson, S. P., and Sigler, P. B. (1996) *J. Mol. Biol. 264*, 1072−1084.
16. Macedo-Riberiro, S., Darimont, B., Sterner, R., and Huber, R. (1996) *Structure 4*, 1291−1301.

17. States, D. J., Haberkorn, R. A., and Ruben, D. J. (1982) *J. Magn. Reson. 48*, 286−292.
18. Marion, D., Ikura, M., Tschudin, R., and Bax, A. (1989) *J. Magn. Reson. 85*, 393−399.
19. Jeener, J., Meier, B. H., Bachmann, P., and Ernst, R. R. (1979) *J. Chem. Phys. 71*, 4546−4553.
20. Macura, S., and Ernst, R. R. (1980) *Mol. Phys. 41*, 95−117.
21. Braunschweiler, L., and Ernst, R. R. (1983) *J. Magn. Reson. 53*, 521−528.
22. Davis, D. G., and Bax, A. (1985) *J. Am. Chem. Soc. 107*, 2820−2821.
23. Griesinger, C., Otting, G., Wüthrich, K., and Ernst, R. R. (1988) *J. Am. Chem. Soc. 110*, 7870−7872.
24. Rance, M., Sørensen, O. W., Bodenhausen, G., Wagner, G., Ernst, R. R., and Wüthrich, K. (1983) *Biochem. Biophys. Res. Commun. 117*, 479−485.
25. Johnson, B. A., and Blevins, R. A. (1994) *J. Biomol. NMR 4*, 603−614.
26. Oschkinat, H., Cieslar, C., Holak, T. A., Clore, G. M., and Gronenborn, A. M. (1988) *Nature 332*, 374−376.
27. Güntert, P., and Wüthrich, K. (1991) *J. Biomol. NMR 1*, 447−456.
28. Wüthrich, K. (1986) *NMR of Proteins and Nucleic Acids*, John Wiley and Sons, New York.
29. Luger, K., Mader, A. W., Richmond, R. K., Sargent, D. F., and Richmond, T. J. (1997) *Nature 389*, 251−260.
30. Kraulis, P. J., Clore, G. M., Nilges, M., Jones, T. A., Pettersson, G., Knowles, J., and Gronenborn, A. M. (1989) *Biochemistry 28*, 7241−7257.
31. Clore, G. M., Appella, E., Yamada, M., Matsushima, K., and Gronenborn, A. M. (1990) *Biochemistry 29*, 1689−1696.
32. Kay, L. E., Forman-Kay, J. D., McCubbin, W. D., and Kay, C. M. (1991) *Biochemistry 30*, 4323−4333.
33. Hol, W. G. J., van Duijnen, P. T., and Berendsen, H. J. C. (1978) *Nature 273*, 443−446.
34. Perutz, M. F., Gronenborn, A. M., Clore, G. M., Fogg, J. H., and Shih, D. T.-B. (1985) *J. Mol. Biol. 183*, 491−498.
35. Shoemaker, K. R., Kim, P. S., Brems, D. N., Marqusee, S., York, E. J., Chaiken, I. M., Stewart, J. M., and Baldwin, R. L. (1985) *Proc. Natl. Acad. Sci. U.S.A. 82*, 2349−2353.
36. Nicholson, H., Becktel, W. J., and Matthews, B. W. (1988) *Nature 336*, 651−656.
37. Sali, D., Bycroft, M., and Fersht, A. R. (1988) *Nature 335*, 740−743.
38. Perutz, M. F., and Raidt, H. (1975) *Nature 255*, 256−259.
39. Nicholls, A. (1993) *GRASP: Graphical representation and analysis of surface properties*, Columbia University, New York.
40. Rees, D. C., and Adams, M. W. W. (1995) *Structure 3*, 251−254.
41. Kellis, J. T., Nyberg, K., Sali, D., and Fersht, A. R. (1988) *Nature 333*, 784−786.
42. Kellis, J. T., Nyberg, K., and Fersht, A. R. (1989) *Biochemistry 28*, 4914−4922.
43. Matsumura, M., Becktel, J. W., and Matthews, B. W. (1988) *Nature 334*, 406−410.
44. Matsumura, M., Wozniak, J. A., Dao-Pin, S., and Matthews, B. W. (1989) *J. Biol. Chem. 264*, 16059−16066.
45. Sandberg, W. S., and Terwilliger, T. C. (1989) *Science 245*, 54−57.
46. Pace, C. N. (1992) *J. Mol. Biol. 226*, 29−35.
47. Kraulis, P. J. (1991) *J. Appl. Crystallogr. 24*, 946−950.
48. Bacon, D. J., and Anderson, W. F. (1988) *J. Mol. Graphics 6*, 219−220.

BI973007A